

PHASE-SENSITIVE AND DUAL-ANGLE RADIOFREQUENCY MAPPING IN
 ^{23}Na MAGNETIC RESONANCE IMAGING

by

Steven P. Allen

A senior thesis submitted to the faculty of

Brigham Young University

in partial fulfillment of the requirements for the degree of

Bachelor of Science

Department of Physics and Astronomy

Brigham Young University

April 2010

Copyright © 2010 Steven P. Allen

All Rights Reserved

BRIGHAM YOUNG UNIVERSITY

DEPARTMENT APPROVAL

of a senior thesis submitted by

Steven P. Allen

This thesis has been reviewed by the research advisor, research coordinator,
and department chair and has been found to be satisfactory.

Date

John Colton, Advisor

Date

Eric Hintz, Research Coordinator

Date

Ross Spencer, Chair

ABSTRACT

PHASE-SENSITIVE AND DUAL-ANGLE RADIOFREQUENCY MAPPING IN ^{23}Na MAGNETIC RESONANCE IMAGING

Steven P. Allen

Department of Physics and Astronomy

Bachelor of Science

Many diagnostic applications in sodium magnetic resonance imaging (MRI) require accurate flip angle mapping. In search for a mapping technique that performs well in sodium MRI, we evaluated the low signal-to-noise ratio performance of the dual-angle and phase-sensitive techniques. Monte Carlo simulations in MATLAB and measurements of a phantom demonstrate the phase-sensitive technique's superior performance in low SNR environments. The phase sensitive technique has a lower standard deviation of measurement and obtains higher quality flip angle maps than the dual-angle technique. Further, *in vivo* maps of the human breast demonstrate the phase-sensitive technique's clinical feasibility

ACKNOWLEDGMENTS

I would like to thank my advisors, Neal Bangerter and John Colton. From getting up in the early hours to go scanning to patiently re-explaining MRI principles, Neal's stubborn dedication, leadership, and advisement made this research possible. Meanwhile, John's feedback and editing has made this thesis possible. I also thank my family. They have proven true and faithful time and again. Their support and love in all areas of my life are invaluable.

Contents

Table of Contents	vi
List of Figures	viii
1 Introduction	1
1.1 Sodium in MRI	1
1.2 A Word on Terminology	3
1.3 Flip-Angle Mapping Techniques	4
1.3.1 Dual-Angle Technique	4
1.3.2 Phase-Sensitive Technique	5
1.4 Sodium Flip Angle Mapping	8
2 Methods	10
2.1 Introduction	10
2.2 Monte Carlo Simulation	11
2.2.1 The Bloch Equations	11
2.2.2 Noise	14
2.2.3 Flip Angle Extraction	14
2.2.4 Simulation	15
2.2.5 Verification	15
2.2.6 Analysis	16
2.3 Phantom Experiments	17
2.3.1 Phantom	17
2.3.2 Scanning Parameters	17
2.3.3 Statistical Analysis	18
2.4 <i>In Vivo</i> Measurements	19
3 Results	20
3.1 Introduction	20
3.2 Scaling	20
3.3 Monte Carlo Simulation	22
3.4 Phantom Measurements	24
3.5 <i>In Vivo</i> Measurements	25

4	Discussion	27
4.1	Consistency In Measurement	27
4.2	Quality Improvement	27
4.3	Effect of Precession During Excitation	28
5	Conclusion	29
A	MRI Basics	31
A.1	Physics	31
A.1.1	Net Magnetization	31
A.1.2	Gyromagnetic Ratio	32
A.1.3	Excitation	33
A.1.4	Precession	34
A.1.5	Decay and Relaxation	34
A.2	Pulse Sequences	35
A.2.1	The Basic Sequence	36
A.2.2	Time Periods	36
A.3	Glossary of Terms	37
	Glossary	40
	Bibliography	40
	Index	42

List of Figures

1.1	Phase accrued as a function of flip angle	5
2.1	Parity between simulation results and expected behavior	16
3.1	Simulation results across all flip angles and values of phase accrued during excitation	21
3.2	Mean and standard deviation of dual-angle and phase-sensitive techniques	22
3.3	Phantom flip angle maps	24
3.4	Phantom standard deviation	25
3.5	<i>In vivo</i> flip angle map	26

Chapter 1

Introduction

1.1 Sodium in MRI

Magnetic resonance imaging (MRI) is a useful tool that utilizes nuclear magnetic resonance (NMR) phenomena to produce images of soft organic tissue. Conventionally, MRI creates these images by using radiofrequency (rf) fields to stimulate and receive information from hydrogen atoms within the body. However, MRI hardware can be adapted to stimulate and receive information from nuclei other than hydrogen—such as fluorine, sodium, and carbon-13. A brief introduction to MRI, including definitions of terms used in this thesis, can be found in Appendix A.

Recent developments in sodium MRI have many useful medicinal applications, including assessing cartilage health [1–4] characterizing and assessing the viability of tumors [5], detecting abnormal sodium levels in the kidneys [6, 7], and assessing tissue damage following stroke [8]. In cartilage, proteoglycans—key to cartilage health and vitality—attract sodium ions into the extracellular matrix. The more proteoglycans, the more sodium within the tissue. Hence sodium concentration measurements can give insight into cartilage composition and health. Likewise, in diseased, tumorous,

or otherwise damaged tissue, the sodium-potassium pump that maintains specific sodium concentration across the cellular membrane functions abnormally, changing the total sodium concentration inside the tissue. The dysfunctional pump causes healthy and diseased tissues that look identical in conventional MRI to carry contrast in sodium MRI.

Accurate quantification of sodium concentration in tissue is of considerable importance for many of the applications listed above [5, 9, 10]. Quantitative analysis of sodium concentration from sodium MRI images requires accurate mapping of the stimulating radiofrequency (rf) field. Measurements of the stimulating radio frequency field are alternately called rf maps or *B1 maps*, where *B1* refers to the magnetic field associated with a stimulating radiofrequency pulse that makes NMR and MRI possible. (We call it a *B1* field because the *B0* field refers to the main polarizing magnetic field and *B* is too ambiguous.)

Currently, there are several challenges to rf mapping in sodium MRI. First, high noise and low signal levels in sodium MRI make accurate mapping in reasonable scan times (ten minutes or fewer) difficult: a sodium scan has ten to twenty times decreased signal-to-noise ratio (SNR) compared to conventional MRI. Increasing time spent scanning can help offset this signal loss, but total recovery of lost SNR leads to prohibitively long scan times.

Further, the problem is compounded by employing rf coil configurations that have significant spatial rf field inhomogeneity. These coils are typically used because their smaller sensitive volume leads to smaller noise sources. However, their high spatial variability in rf field strength distorts sodium concentration analysis. In MRI, signal magnitude is a function of rf magnitude in addition to sodium concentration. Hence, tissues with equal sodium concentration can appear to have different concentrations because the rf amplitude varies between their locations.

Fully realizing sodium MRI as a clinical diagnostic tool requires accurate rf mapping in low SNR environments and across high spatial rf variability. In this thesis, we compare two rf mapping techniques and analyze their performance in low SNR situations.

1.2 A Word on Terminology

As mentioned in the appendix, the word *flip angle* corresponds to the angle made between the tissue magnetization's orientation before excitation by the rf field and its final orientation after excitation by the rf field. It plays a crucial role in MRI processes.

Throughout the literature, the terms *flip angle map* and *B1 map* are used interchangeably. This is because the stimulating rf field strength and the resulting flip angle it creates are, to first approximation, linearly proportional to each other. For flip angles of 0 to 180 degrees, the flip angle α can be very closely approximated by the equation:

$$\alpha = \gamma \int_0^{\tau} B1 dt. \quad (1.1)$$

where γ is the *gyromagnetic ratio* (see Appendix A for an introduction) and $B1$ and τ are the strength and length of the rf pulse respectively.

Assuming the rf pulses have very slow amplitude variations in time, the flip angle is linearly dependant on B1 strength. Hence, in this regime, a flip-angle map is merely a B1 map multiplied by a constant τ . In this thesis we will follow the literature and use flip-angle map synonymously with B1 map, since most sodium quantization applications are primarily concerned with relative variations in rf field strength rather than absolute strength.

1.3 Flip-Angle Mapping Techniques

We seek a flip angle mapping technique that gives the best possible performance in low-signal, high-noise situations. As a part of this search, we compare the performance of two flip angle mapping techniques: the *dual-angle technique* and the *phase-sensitive technique*. The dual angle technique is much older and commonly used in sodium flip angle mapping; the phase sensitive technique is more recent and shows promise for superior high noise performance [11].

1.3.1 Dual-Angle Technique

The dual-angle technique derives flip angle information from the relationship of two images. These images are acquired when the amplitude of the stimulating rf field for the second image is set to twice the amplitude of the field used for the first image. This 1:2 ratio allows the flip angle α to be extracted by the equation

$$\alpha = \arccos \left[\frac{M2}{2M1} \right] \quad (1.2)$$

where $M1$ is the magnitude of the first acquisition, and $M2$ is the magnitude of the second acquisition [12–14].

This technique is useful because the flip angle estimate is given by a monotonically decreasing function. In other words, each unique value returned by the ratio $\frac{M2}{2M1}$ links to a unique flip angle. Further, calculating a ratio of image magnitudes is computationally inexpensive.

However, the dual-angle technique also has drawbacks. The technique is inaccurate at flip angles below 20 degrees. As both $M1$ and $M2$ are very small in this situation, variations due to noise in either value can cause large variations in their ratio. As will be seen in Chapter 3, this behavior will lead to systematic errors in the flip angle estimate at low flip angles.

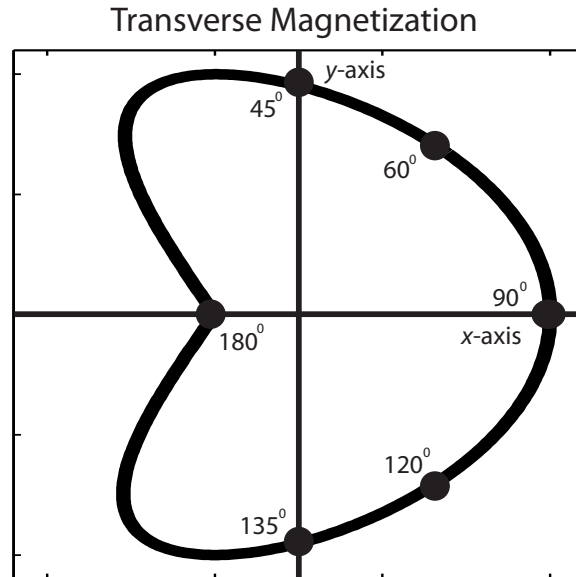


Figure 1.1 The resulting magnetization in the x-y plane after a phase-sensitive sequence for various flip angles.

Further, $M1$ and $M2$ are always positive values. With no possibility for a negative argument, the arccos function effectively limits the dual-angle technique to a dynamic range of 20° to 90° .

1.3.2 Phase-Sensitive Technique

While the dual-angle technique encodes flip angle information in the ratio of two acquisition magnitudes, the phase-sensitive technique encodes flip angle information in the difference of phase between two acquisitions. The sequence for encoding flip angle into signal phase is somewhat more complicated than the sequence for the dual-angle technique.

Suppose the magnetization vector is oriented along the z direction before excitation. The phase-sensitive technique begins with an rf pulse that tips the magnetization vector 2α about the x -axis. Once completed, the magnetization vector is again flipped α about the y -axis. Should α be 90° , the magnetization will then be aligned

completely along the x -axis. This corresponds to a signal with zero relative phase to the x -axis. However, should α be any value other than 90° , the magnetization will be aligned somewhere between the x and y -axes, and the resulting signal will have accumulated phase relative to the x -axis. Fig. 1.1 plots the phase-sensitive signal phase as a function of several flip angles. As can be seen, the value of this phase scales with the difference between α and 90° .

Unfortunately, for this sequence, there are factors other than just flip angle that lead to signal phase. When unaccounted for, they introduce error into the phase-sensitive flip-angle measurement. Such factors include off-resonant precession due to B0 inhomogeneity, retarded potentials, and chemical shift. They must be taken into account before accurate flip angle information can be derived from the signal phase.

We can eliminate most of these signal phase sources by acquiring a second image using a sequence that is identical to the 2α - α pulse described above except for a -2α initial pulse about the x axis rather than a $+2\alpha$ pulse. After excitation, the $\pm 2\alpha$ sequences each accrue equivalent values of phase. Subtracting the phase from the two acquisitions subtracts out phase that has accrued after excitation.

The signal phase accrued during excitation is more difficult to eliminate. The $\pm 2\alpha$ pulses acquire different amounts of phase during excitation and simple subtraction fails to eliminate all of the accrued signal phase. However, the signal phase can be described as a function of both the flip angle and phase accrued during excitation. If the amount of phase accrued during excitation can be predetermined, flip angle information can still be extracted from the signal phase.

Consider a volume of tissue where the B0 field strength is slightly different relative to the field strength in the surrounding tissue. The net magnetization of that volume precesses at a different rate, ω , relative to the surrounding tissue. The phase acquired during a particular rf pulse is then described by $\omega\tau$, where τ is the duration of the rf

pulse.

Morrell found that, with B0 inhomogeneity, the magnetization vectors of a single acquisition are described by

$$M_x^\pm = \pm \frac{M_0 \alpha \omega \tau}{\beta^2} (4 \sin^2 \beta \cos \beta) - \frac{M_0 \alpha \sin \beta}{\beta^3} (\alpha^2 \cos 2\beta + \omega^2 \tau^2) \quad (1.3)$$

$$M_y^\pm = \pm \frac{M_0 2\alpha \sin \beta}{\beta^3} (\omega^2 \tau^2 \cos^2 \beta + \alpha^2 \cos \beta) + \frac{M_0 \alpha \omega \tau}{\beta^4} (1 - \cos \beta) (\alpha^2 \cos 2\beta + \omega^2 \tau^2) \quad (1.4)$$

The subtracted signal phase Φ used to extract flip angle information is found by

$$\Phi = \angle M_{xy}^+ - \angle M_{xy}^- \quad (1.5)$$

where M_0 is the magnetization strength, M_{xy}^\pm is the combined x and y component of the magnetization vector, α is the flip angle, $\omega\tau$ is as described above, and β is equal to $\sqrt{\alpha^2 + \omega^2 \tau^2}$. The \pm sign refers images acquired by the positive and negative initial 2α sequenc respectively [11].

As mentioned above, the subtracted phase Φ is ideal for flip angle extraction because it either accounts for or eliminates sources of accrued phase other than the flip angle. However, analytically extracting the flip angle from Eq. (1.5) is exceedingly complicated. Morrell suggests using a previously-computed lookup table giving α as a function of $\omega\tau$ and Φ to extract flip angle information [11]. In the following chapters, all phase-sensitive flip angle maps employ lookup tables to extract the flip-angle from the subtracted phase.

The phase-sensitive technique exhibits greater dynamic range than the dual-angle technique since it assigns unique phase values to flip angles between 0 and 180°. It also only introduces systematic error at flip angles of 10° and lower.

However, the phase-sensitive technique is computationally expensive. Further, large variations in B0 strength and large flip angles can cause Φ to *wrap*, meaning

phase values greater than 2π radians are inadvertently mapped to values between 0 and 2π radians. This effect can be solved by employing a phase unwrapping algorithm, though such algorithms can also be computationally expensive. Further, the 180° pulses emit large amounts of rf energy which can cause tissue heating and possible damage.

The phase-sensitive technique also becomes inaccurate as phase accrued during excitation becomes increasingly large. In this case, the subtracted phase given in Eq. 1.5 ceases to be a monotonic function of flip angle. This means that particular values of the subtracted phase simultaneously correspond to several different flip angles. The lookup table algorithm cannot distinguish between these possible values and usually picks the first and—often times—incorrect match.

Though these issues can be relieved through high-speed processing, robust phase-unwrapping algorithms, and reduced-amplitude rf pulses, they cause the phase-sensitive technique to be much more complicated and technical than the dual-angle technique.

1.4 Sodium Flip Angle Mapping

Given sodium's lower gyromagnetic ratio (approximately 1/4 that of hydrogen) and the corresponding reduction in relative precession rates, the phase-sensitive B1 mapping technique seems a good candidate for flip angle mapping in sodium MRI. However, its ability to perform well in high noise environments or over large B1 variations endemic to sodium MRI has yet to be demonstrated.

In this work we evaluated the performance of both techniques in high noise situations. We found that the phase-sensitive technique was much better at dealing with high noise situations than the dual-angle technique. Our analysis was accomplished through computer simulations, phantom measurements, and *in vivo* measurements.

The phantom measurements and Monte Carlo simulations demonstrated that the phase sensitive technique performs more accurately in low noise environments than the dual-angle technique. Further, *in vivo* measurements demonstrate that the phase-sensitive technique can be applied in a clinical setting and in reasonable scan times.

Chapter 2

Methods

2.1 Introduction

As stated in Chapter one, we compared the low SNR performance between the dual-angle and phase-sensitive flip-angle mapping techniques. We found that the phase-sensitive technique was much better at dealing with high noise situations than the dual-angle technique. We arrived at this conclusion through three experimental methods: computer simulations, phantom measurements, and an *in vivo* scan.

First, we designed an algorithm (often called a Monte Carlo simulation) in MATLAB to simulate the noise-corrupted flip-angle estimate returned by each flip-angle mapping technique. The resulting mean and standard deviation calculated from 10,000 iterations of this simulation predicted the phase-sensitive technique's superior performance in a noisy environment.

Then, we corroborated the results of the Monte Carlo simulations with a series of flip-angle maps formed by phantom scanning. A phantom is some sort of object that mimics MRI properties of living tissue. Phantoms simulate clinical experiments without the added cost and complexity of human subject scanning. The mean and

standard deviation across the phantom series verified our predictions made by the Monte Carlo simulations.

Lastly, we demonstrated the phase-sensitive technique in a human-subject (*in vivo*) scan. *In vivo* scans suffer from lower SNR than phantom scans and are more difficult to accomplish. Breathing, fluid flow, and eddy currents common to living tissue distort image data. Successful implementation in the *in vivo* environment is the ultimate test of any technique used in MRI. Our *in vivo* scan showed the phase-sensitive technique's robustness and practicality in a clinical environment.

The details of the three methods are described below.

2.2 Monte Carlo Simulation

Computer simulations are often an effective way to model physical systems and predict their future behavior. I adapted a common MRI model to the phase-sensitive and dual-angle flip-angle mapping techniques. I then created a MATLAB program to evaluate this model's performance in low SNR situations.

2.2.1 The Bloch Equations

The physics of NMR can be phenomenologically described by the *Bloch equations*. These equations describe how the net magnetic moment of a small volume of tissue (called a *voxel*) will behave under various situations common in MRI such as excitation by an rf pulse, precession under a magnetic field, transverse decay (often labeled *T2 decay*) and longitudinal relaxation (*T1 relaxation*). The exact form of these equations as well as several solutions can be found in any introductory MRI or NMR reference such as Nishimura [15] and Bernstein et al. [16].

My simulations used solutions to the Bloch equations to calculate the net magne-

tization of a given voxel of tissue as it progresses through each stage of each flip-angle mapping technique. By varying different MRI parameters I was able to examine the performance of each technique in low SNR situations.

In my simulation, I used a three-element vector to represent the x , y , and z components of a voxel's net magnetization. This mathematical set-up is convenient because solutions to the Bloch equations are easily represented by 3×3 matrices. For example, a flip of angle α about the x axis can be represented by the matrix

$$\mathbf{M} = \begin{bmatrix} 1 & 0 & 0 \\ 0 & \cos \alpha & -\sin \alpha \\ 0 & \sin \alpha & \cos \alpha \end{bmatrix} \quad (2.1)$$

and the net magnetization, M' , resulting from such a flip acting on a magnetization vector M is found by

$$\begin{bmatrix} M'_x \\ M'_y \\ M'_z \end{bmatrix} = \begin{bmatrix} 1 & 0 & 0 \\ 0 & \cos \alpha & -\sin \alpha \\ 0 & \sin \alpha & \cos \alpha \end{bmatrix} \times \begin{bmatrix} M_x \\ M_y \\ M_z \end{bmatrix} \quad (2.2)$$

where M_x , M_y , and M_z are respectively the x , y , and z components of an arbitrary magnetization vector.

Other matrices, such as those used to describe precession due to off-resonant precession frequency, excitation about any arbitrary axis, and relaxation and decay can also be found in Nishimura [15]. Complex sequences can be calculated by multiplying the appropriate matrices in sequence with the magnetization vector.

My simulations consisted of combining these matrices together to simulate the phase-sensitive and dual-angle techniques. For example, I described the dual-angle

technique by the matrix

$$\begin{bmatrix} M'_x \\ M'_y \\ M'_z \end{bmatrix} = \mathbf{A}_{\text{te}} \times \mathbf{T}_\alpha \times \begin{bmatrix} 0 \\ 0 \\ M_z \end{bmatrix} + \mathbf{B}_{\text{te}} \quad (2.3)$$

In this equation we assume time between readout and excitation is usually so long the magnetization has fully relaxed in the z direction to its original strength, M_z . The matrix \mathbf{T}_α tips the initial magnetization vector $(0, 0, M_z)$ around the y -axis. Meanwhile, the matrices \mathbf{A}_{te} and \mathbf{B}_{te} describe precession, decay, and relaxation from the moment of excitation to the moment of readout. In essence, the equation gives the magnetization vector at readout, after relaxing in the z direction, being tipped about the y -axis, and then precessing and decaying before the moment of readout.

The following equation simulated the phase-sensitive technique.

$$\begin{bmatrix} M'_x \\ M'_y \\ M'_z \end{bmatrix} = \mathbf{A}_{\text{te}} \times (\mathbf{T}_\alpha \times \mathbf{A}_{\text{tflip}} \times [\mathbf{T}_{2\alpha} \times \begin{bmatrix} 0 \\ 0 \\ M_z \end{bmatrix}] + \mathbf{B}_{\text{tflip}}) + \mathbf{B}_{\text{te}} \quad (2.4)$$

The matrices \mathbf{A}_{te} and \mathbf{B}_{te} , as well as the value M_z , have the same meaning as those used in the dual angle algorithm. The matrices \mathbf{T}_α and $\mathbf{T}_{2\alpha}$ correspond to the initial 2α flip about the y -axis and the subsequent α flip about the x -axis. Meanwhile, $\mathbf{A}_{\text{tflip}}$ and $\mathbf{B}_{\text{tflip}}$ allow for precession and decay between excitation pulses. In essence, this equation gives the magnetization of a vector that has grown along the z -axis from zero, been flipped, precessed and relaxed, flipped again, and then allowed to precess and relax until the moment of readout.

The magnitude and phase of the NMR signal in the receiver coil are directly proportional to the magnitude and phase of the magnetization vectors (M_x and M_y) at readout. Hence, the phase and magnitude of the x and y components of Eqs. (2.3)-

(2.4) effectively give the readout signal.

2.2.2 Noise

In NMR, most signal noise arises from eddy currents and thermal motion within the tissue. The effects of noise on the voltage signal recorded by the scanner have been experimentally shown to behave as random, independent Gaussian variables with zero mean [15]. These random variables add to the M_x and M_y vector components independently. For each iteration of the simulation, I used MATLAB's random number generator to assign unique noise values to the M_x and M_y values resulting from Eqs. (2.3)-(2.4). According to convention I based the standard deviation, σ , of these random numbers on the equation

$$\sigma = M/S \tag{2.5}$$

where M is the largest possible signal magnitude, and S is the signal-to-noise ratio. This equation is chosen because both M and S are good estimates of the intensities of the respective image and noise signals.

In the simulation, SNR levels were chosen to be 10, 15, and 20. These levels are typical of sodium MRI [17].

These noise values added to the xy components of Eqs. (2.3)-(2.4) comprise my model for both flip angle mapping techniques.

2.2.3 Flip Angle Extraction

With Eqs. (2.3)-(2.4) giving the tissue magnetization at readout, flip angle information can be extracted by means of Eq. (1.2) (dual-angle technique) or a lookup table (phase-sensitive technique).

2.2.4 Simulation

I created a MATLAB algorithm that used the models described above to compute 10,000 noise-corrupted flip-angle estimates for each mapping technique. Additionally, I assigned the algorithm T1, T2, TR, TE, and Tflip values of 50, 50, 100, 10, and 0.01 milliseconds, respectively. The T1 and T2 values were chosen to closely mimic values measured in sodium experiments. Likewise, the TE, TR, and Tflip values were chosen to match those used in my subsequent phantom experiments. I also assigned phase accrued during excitation to values ranging from -180° to 180° .

I chose to simulate the phase-sensitive technique across input flip angle values of 0 to 180° and the dual-angle technique across a range of 0 to 90° . As discussed in Chapter 1, these flip angles comprise the limits of each technique's dynamic range. Hence, the range of input flip angles used in the simulation comprise all possible input flip angles for which each techniques utilize to give a valid estimate.

The algorithm computed 10,000 noise corrupted flip-angle estimates for each possible input flip angle as well as over a every possible value of phase accrued during excitation.

2.2.5 Verification

It can often be difficult to verify if a Monte Carlo simulation is exactly mimicking the physical process one intends it to mimic. Hence, the interesting results that a simulations yields may actually have no correlation to reality. Our Monte Carlo simulation was verified by simulating the performance of each technique with the noise factor discussed in section 2.1.2 turned off.

Fig. 2.1 shows the result in this verification process. Both techniques behave as described in Chapter 1: The dual-angle technique shows that it only can be applied

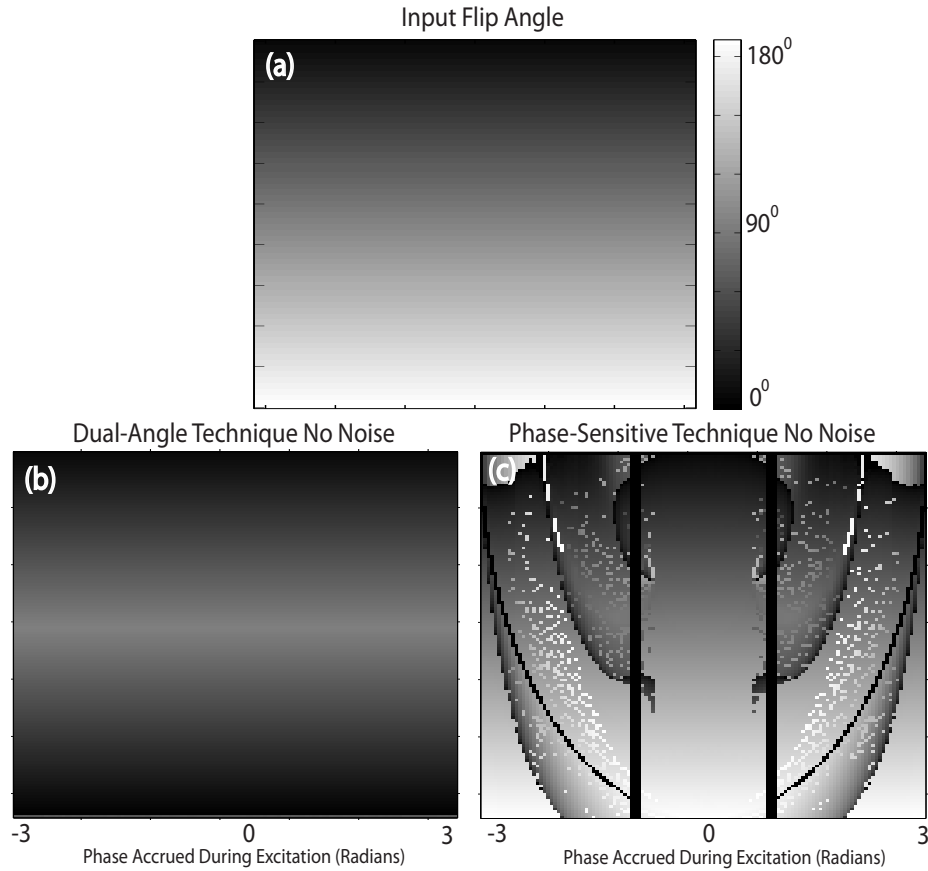


Figure 2.1 Agreement between the (a) input flip angle and flip angle estimates made by (b) the dual-angle technique and (c) the phase-sensitive technique.

across a flip angle range of $0\text{-}45^\circ$, and is not sensitive to phase accrual during excitation. The phase-sensitive technique returns valid results over a range of $0\text{-}180^\circ$, but displays sensitivity to phase acquired during excitation. In the no-noise environment, the algorithm accurately reproduces the previously described behavior of each technique. It appears to follow the physical process of the pulse sequence.

2.2.6 Analysis

Statistical mean and standard deviation of the simulation's results were then computed. Their significance will be discussed in Chapter 3.

2.3 Phantom Experiments

I then corroborated the results of the Monte Carlo simulations with a statistical analysis of a series of phantom measurements. These phantom measurements consist of inserting a phantom into the scanner and using the appropriate scanning sequence to obtain flip-angle maps. I obtained 16 flip-angle maps from each sequence and compared the resulting mean and standard deviation.

2.3.1 Phantom

Our phantom is a 14 inch long, three inch wide cylindrical bottle filled with water and doped with 200mM sodium concentration. The 200mM concentration matches concentration values found in cartilage [18].

2.3.2 Scanning Parameters

Scanning in MRI is significantly more complicated than theoretical simulations. Scanning involves advanced signal processing, Fourier transforms, and manipulation of the main magnetic field. A detailed explanation of this process is beyond the scope of this thesis and can be found in MRI reference manuals such as in Nishimura [15] and Bernstein [16]. However, a brief introduction to the parameters used in the phantom scans and their effect on the resulting flip-angle map is given below.

I implemented both B1 mapping techniques using identical *3D EPI* sequences adapted for sodium imaging on a 3T Siemens Trio MRI scanner (Siemens Medical Systems, Erlangen, Germany).

The acronym EPI stands for echo planar imaging and merely identifies the rate and pattern in which image information is sampled. Different sampling sequences have different strengths and weaknesses. The EPI sequence rapidly acquires image

data but is sensitive to distortion effects (called *artifacts*). I used the same EPI sequence for both techniques to preserve these weaknesses and strengths across all images.

Matrix size (the dimensions of the flip-angle map) and field of view (FOV) determine the dimensions of a given flip-angle map and its resolution (centimeters per voxel). These two parameters control to which part of the phantom each voxel corresponds.

Readout duration and readout bandwidth determine the time a sequence takes to acquire a complete set of image data and the frequency range accepted by the receiving coil, respectively. SNR is directly proportional to the square root of readout duration and inversely proportional to the square root of readout bandwidth.

Maintaining identical matrix size and voxel size across all 32 flip-angle maps of the phantom ensured that any voxel on one map corresponded to the same voxel on any other flip-angle map. Further, keeping identical total readout duration (total time spent acquiring image information), and readout bandwidth across all acquisitions maintained comparable SNR levels in each acquisition.

Each of the 32 flip-angle maps were obtained with the following parameters: TR=100ms, TE=15 ms, EPI factor=3 (pertinent to the sampling sequence), FOV=11.2×19×10 cm, matrix size=38×64×20, readout bandwidth=165 Hz/pixel, total scan time=5 m 20 s.

2.3.3 Statistical Analysis

Statistical mean and standard deviation across the sixteen images for each respective technique were calculated in MATLAB. SNR was also computed and shown to be almost comparable across most samples (see section 4.3 for discussion).

2.4 *In Vivo* Measurements

No amount of theoretical work in MRI is useful without clinical application. Implementation is the net end and grand design for any development in MRI. Therefore, the phase-sensitive technique was put to the test in an *in vivo* breast scan. *In vivo* scans demonstrate the phase-sensitive technique's feasibility in a clinical setting.

In vivo experiments were chosen in the human breast for two reasons: Fibroglandular tissue in the human breast contains higher concentrations of sodium than knee cartilage, brain matter, and most other tissues. Higher concentrations lead to higher SNR which makes a challenging imaging technique easier. The higher sodium concentrations in fibroglandular tissue also make the technique particularly ideal for characterizing breast tumors. Secondly, the breast is also larger than other tissues with high concentrations of sodium, making it easier to map out a spatially varying rf field.

In order to complete a successful flip-angle map in living tissue, we had to make several modifications to the sequence used in section 2.2. *In vivo* scans suffer from severe signal degradation due to eddy currents, ion motion, and thermal noise in the tissue. In order to prepare for this serious signal loss, we employed a coil with a diameter reduced by one quarter, we quadrupled the total readout time, and doubled voxel size in one dimension. Each of these modifications increases SNR by two for a total increase in SNR of eight.

In vivo measurements in the breast were obtained from a volunteer according to IRB standards. The 3D EPI sequence had the following parameters: TR=100ms, TE=9 ms, EPI factor=3, FOV=25.6×25.6×32 cm, matrix size=64×64×32, readout bandwidth=165 Hz/pixel, total scan time=9 m 22 s.

Chapter 3

Results

3.1 Introduction

In Chapter 2 we discussed the three methods used to compare the phase-sensitive technique to the dual-angle technique. Here, I present and explain the results of these methods. Before examining these results, however, I first explain an apparent scaling discrepancy between flip angle maps made by the dual-angle technique and those made by the phase-sensitive technique.

3.2 Scaling

In the preceding experiments, doubling the flip angle is accomplished by doubling the strength of the rf field. Therefore, as the nominal flip angle for the phase-sensitive technique is twice that of the dual-angle technique (90 degrees for the phase-sensitive technique and 45 degrees for the dual-angle technique), the rf field measured by the phase-sensitive technique is twice that of the field measured by the dual-angle technique. Hence, a unit variation of field magnitude seen by the dual-angle technique

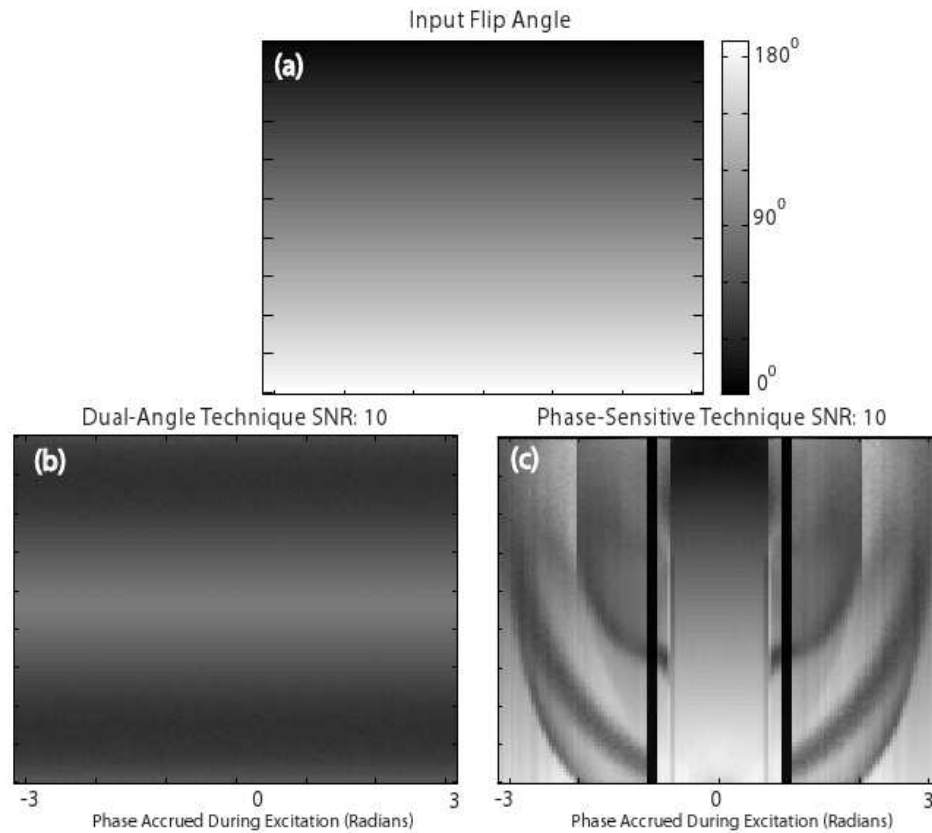


Figure 3.1 Comparison between (a) input flip angle and flip angle estimates made by (b) the dual-angle technique and (c) the phase-sensitive technique.

is seen as a variation of two units by the phase-sensitive technique. In flip angle map terms, a variation of one degree for the dual-angle technique corresponds to a variation of two degrees for the phase-sensitive technique.

Fortunately, the phase-sensitive technique has a built in scaling factor that corrects for this difference in scaling. The phase-sensitive technique can measure twice the range of flip angles than that of the dual-angle technique. Scaling each image to its respective technique's applicable range effectively divides the flip angle maps produced by the phase-sensitive technique by two. Hence, though flip angle maps produced by each technique have different ranges, relative shading across each image corresponds

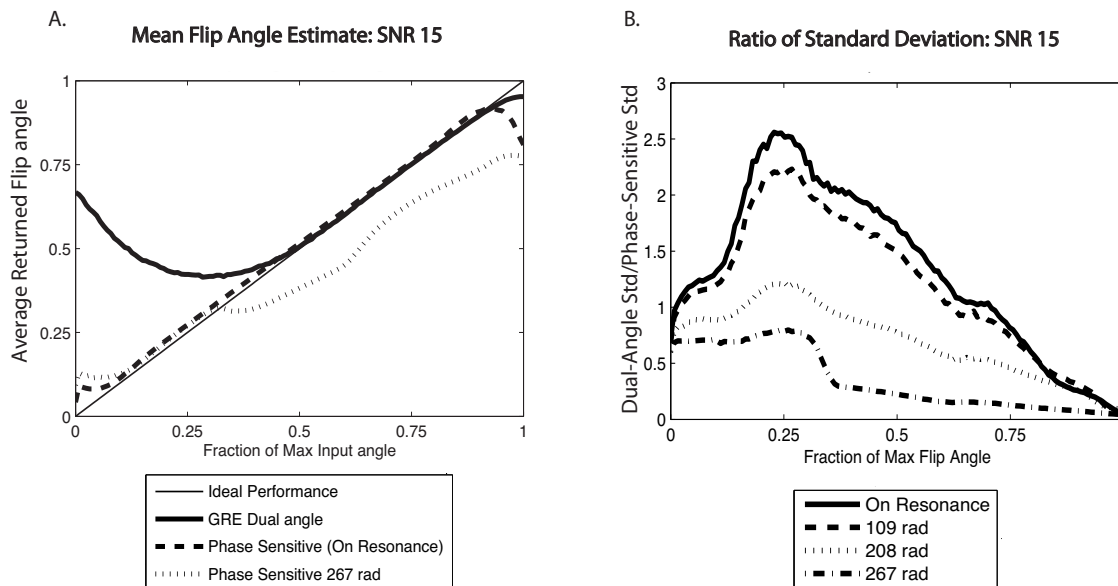


Figure 3.2 (A) Average of ten thousand flip-angle estimates by the phase-sensitive technique and the dual-angle technique for various amounts of phase accrued during excitation. (B) Ratio of the standard deviation of the dual-angle technique to the standard deviation of the phase-sensitive technique. Each line corresponds to a specific amount of phase accrued during excitation.

to equivalent variations in rf magnitude.

The following phase-sensitive flip angle maps have twice the scaling range of the dual-angle flip-angle maps. However, their relative shading shows equivalent levels of rf variation.

3.3 Monte Carlo Simulation

Results from the Monte Carlo simulations discussed in Chapter 2 are recreated in Fig. 3.1 and Fig. 3.2. The plot in Fig. 3.1(a) represents the algorithm's input flip angle. An ideal flip angle mapping technique would perfectly recreate this map. Figs 3.1(b)-(c) show the dual-angle and phase-sensitive techniques' flip-angle estimate in comparison to the input flip angle. In this figure, values along the y -axis correspond

to the algorithm's input flip angle. Values along the x -axis correspond to phase accrued during excitation. Image magnitude corresponds to the algorithm's output flip angle. Neither flip-angle mapping technique is capable of returning accurate estimates for all possible flip angles and possible values of phase accrued during excitation. The dual-angle technique cannot give accurate flip-angle estimates for flip angles greater than 90° . Meanwhile, the phase-sensitive technique becomes very inaccurate for large values of phase accrued during excitation.

The large black bars in Fig. 3.1(c) occur when the first available match between the lookup table and the calculated subtracted phase value is a flip angle of zero degrees.

In Fig. 3.2(a), the average, noise-corrupted flip angle estimate returned from the Monte Carlo simulations for both techniques is plotted as a function of input flip-angle. The x and y axes give input and returned flip angles as a fraction of each technique's respective maximum flip angle. Both techniques have a systematic error for low input flip angles. Also, the phase-sensitive flip angle estimate is again shown to develop significant error as phase accrued during excitation becomes large.

Standard deviation of the noise-corrupted flip angle estimates given by the Monte Carlo simulations are reported in Fig. 3.2(b). This figure plots the standard deviation of the dual-angle technique divided by the standard deviation of the phase-sensitive technique. Each line on the graph corresponds to a specific value of phase accrued during excitation. The phase-sensitive technique has smaller variation of measurement for a wide range of flip angles. However, this advantage is lost as phase accrued during excitation becomes large.

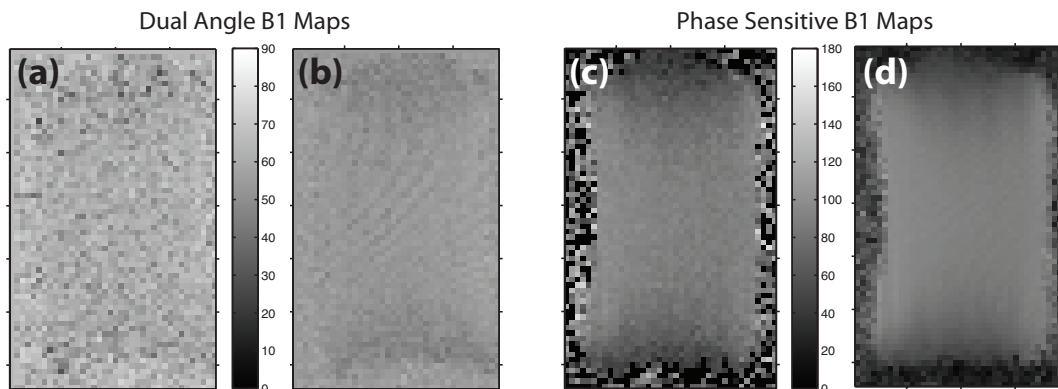


Figure 3.3 (a) single flip-angle map and (b) average of 16 dual-angle acquisitions. (c) single flip-angle map and (d) average of sixteen phase-sensitive acquisitions. Note the phase-sensitive technique’s robustness in high noise situations.

3.4 Phantom Measurements

Sample sodium flip angle maps of the phantom for each technique are shown in Fig. 3.3. Maps from a single acquisition for each technique are shown in Fig. 3.3(a) and Fig. 3.3(c), while the resulting means across the 16 measurements are shown in Fig. 3.3(b) and Fig. 3.3(d). The mean flip angle maps of both techniques exhibit rf shading consistent with previous coil studies where coil geometry and makeup are similar to those used in this phantom study [12]. This confirms the assertion that the phase-sensitive technique yields comparable flip angle information to the dual-angle technique.

The superior performance of the phase-sensitive technique is clearly visible in Figs. 3.3(a) and (c). The phantom image in the phase-sensitive technique emerges well above the noise floor (the noisy background of the flip angle map) while the dual-angle map is nearly buried in noise. The ripples visible in all four figures are caused by the EPI sequence employed while scanning.

Corresponding standard deviation maps of the 16 measurements are shown in

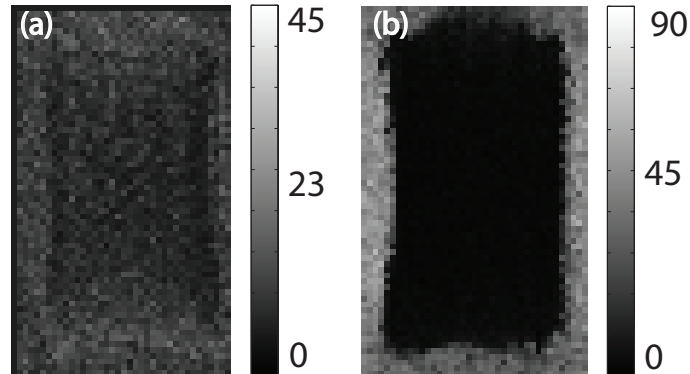


Figure 3.4 Standard deviation of 16 (a) dual-angle and (b) phase-sensitive flip angle maps. The phase sensitive technique is more likely to yield accurate measurements in low SNR situations.

Fig. 3.4. As can be seen, the phase-sensitive technique has a consistently lower standard deviation of measurement than the dual-angle technique. This means the phase-sensitive technique performs much more consistently than the dual-angle technique. This is consistent with my Monte Carlo simulations [Fig. 3.2(b)].

3.5 *In Vivo* Measurements

A phase-sensitive sodium flip-angle map of the breast is shown in Fig. 3.5 along with a hydrogen and sodium magnitude image. Though image SNR is below 30, the technique gives smooth flip angle maps well above the noise floor. Further, the image was obtained in under ten minutes. Hence, the phase-sensitive technique performs well enough to provide valuable information on sodium flip angle variations across breast tissue in reasonable scan times. Achieving usable sodium B1 maps *in vivo* with the dual-angle technique typically requires prohibitively long scan times. As shown, the phase-sensitive technique is able to provide useful clinical sodium flip-angle maps in acceptable scan times.

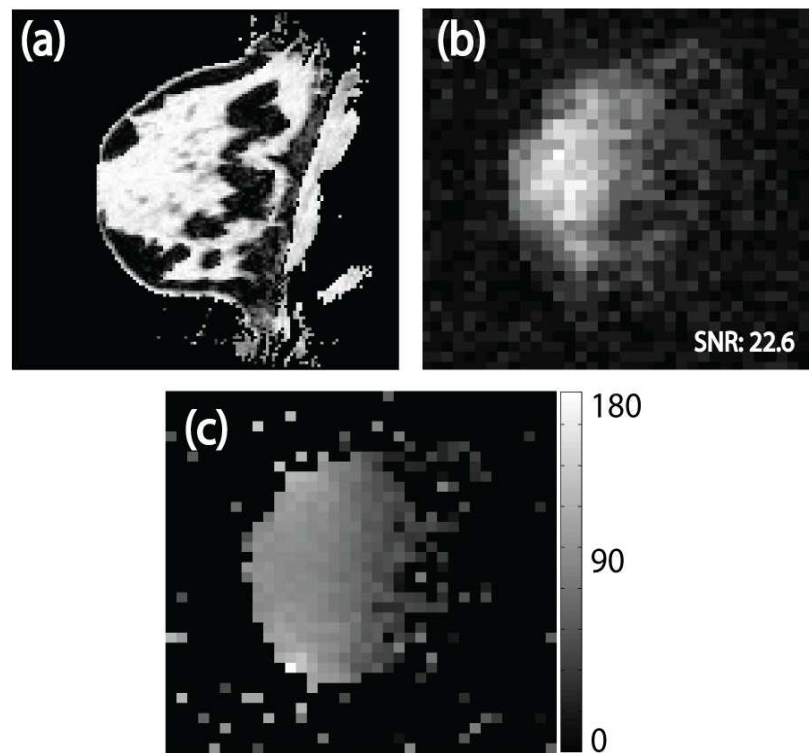


Figure 3.5 (a) Hydrogen image of the human breast. (b) Accompanying sodium magnitude image and (c) phase sensitive flip angle map.

Chapter 4

Discussion

4.1 Consistency In Measurement

Our results (both theoretical and measured) indicate that the phase-sensitive and dual-angle techniques achieve equivalent flip angle measurement in sodium MRI. However, the phase-sensitive technique demonstrates a significantly and consistently lower standard deviation of measurement and much better noise performance. This confirms previous theory [11], and suggests that using the phase-sensitive technique to acquire quality flip-angle maps in reasonable scan times is feasible for clinical sodium MRI.

4.2 Quality Improvement

While promising, the *in vivo* map presented in Fig. 3.5 is still quite noisy. The EPI sequence is far from optimal due to rapid T2 decay and the long echo time (TE) required by the trajectory. Using SNR-efficient pulse sequences such as 3D twisted projection imaging (3D TPI) and the 3D cones sequence should significantly improve

flip-angle map quality [19–21].

4.3 Effect of Precession During Excitation

The simulations presented in Chapter 2 demonstrate a significant degradation in phase-sensitive technique performance as phase accrued during rf excitation becomes large. The small gyromagnetic ratio of sodium relative to that of hydrogen makes this degradation less of an issue in sodium flip-angle mapping. However, in situations where unusually large amounts of phase accrual are expected, performance gains of the phase-sensitive technique over the dual-angle technique reduce or disappear entirely.

We have noted during our phantom experiments that phase sensitive images corresponding to positive and negative initial 2α flips exhibit different SNR levels. Assuming equivalent noise levels, SNR can only change across acquisitions when the maximum image amplitude varies. However, for the phase-sensitive technique, signal magnitude in positive and negative acquisitions is equivalent unless the magnetization vector precesses during excitation. This unaccounted precession introduces a small systematic error into the phase-sensitive flip-angle estimate for each acquisition of the phantom.

While this precession was relatively small, further refinement and improvement could exploit a B0 map (and corresponding corrections to the lookup table that yields flip angle from phase) to achieve more accurate measurement of the flip-angle with the phase-sensitive technique.

The *in vivo* flip angle estimates by the phase-sensitive technique discussed in section 2.4 have compensated for this effect by measuring the B0 inhomogeneity across the phantom and appropriately modifying the lookup table algorithm.

Chapter 5

Conclusion

In a sodium MRI environment, the phase-sensitive technique for flip angle mapping has been shown to return comparable flip angle values with the dual-angle technique while maintaining greater consistency in measurement. This superior performance is demonstrated through Monte Carlo simulations and phantom measurements, while the feasibility of the technique is demonstrated through *in vivo* acquisitions.

Monte Carlo simulations show that flip angle maps made by the phase-sensitive technique have a similar mean, though smaller standard deviation, at low SNR compared to those of the dual-angle technique. Further, the phase-sensitive technique can image a larger dynamic range of rf inhomogeneity than the dual angle technique for small flip angles. This superior performance remains consistent though a wide amount of phase accrued during excitation.

Theoretical results of the Monte Carlo simulation have been corroborated with phantom experiments. A single flip angle map of a phantom acquired by the phase-sensitive technique versus a single flip angle map of the dual-angle technique demonstrates a clear difference in high-noise performance and measurement consistency. Further, standard deviation of phase-sensitive measurements is consistently smaller

than that of the dual-angle technique across the body of the phantom. The phase-sensitive technique is less susceptible to noise effects than the dual-angle technique in the low SNR environment of sodium MRI.

In vivo measurements show that the phase-sensitive technique can be applied in a clinical environment. These measurements employ a 3D EPI sequence which causes near prohibitively long scan times and a certain amount of image artifacts. Though immediately feasible, *in vivo*, phase-sensitive flip-angle mapping in sodium MRI stands to improve from more SNR-efficient pulse sequences and improvements in readout hardware.

Appendix A

MRI Basics

A.1 Physics

The following section presents the basic physics of MRI. Many unfamiliar terms listed in the body of the thesis can be found here.

A.1.1 Net Magnetization

The math that is used to formulate quantum mechanics gives rise to the non-intuitive concept of quantum numbers. These are a series of numbers that govern physical properties and behavior of very small particles. One of these numbers is called *spin* because the larger the number, the more angular momentum the particle has. Nuclei with spin also have a net magnetic moment. In other words, they behave as if they are microscopic magnets. Hydrogen and sodium have spin $\frac{1}{2}$ and spin $\frac{3}{2}$ respectively and have corresponding net magnetic moments.

In most situations, the magnetic moments of sodium that are scattered throughout tissue orient themselves randomly; any magnetic field created by one nucleus is promptly canceled out by the other nuclei placed nearby. Hence, tissue is ordinarily

non-magnetic. However, when placed in a large external magnetic field, the magnetic moments tend to align with the field. This alignment of large numbers of microscopic magnets creates a large net magnetic moment within the tissue. MRI scanners use superconducting wires to create the very powerful magnetic fields necessary to align nuclei within the body and create a large net magnetization.

Fortunately, the magnetic field in medical scanners is strong enough to align very large numbers of nuclei even within a very small *voxel* (a 3D volume) of tissue. In this case, the net magnetization of each voxel obeys *Bloch equations*. These classical equations express how the net magnetization precesses, rotates, and returns to its original orientation based on the direction and strength of the external magnetic field. They can be found in any introductory MRI text book such as Nishimura [15] and Bernstein [16].

A.1.2 Gyromagnetic Ratio

Before we go further, it is important to note the role of the *gyromagnetic ratio* in MRI. This ratio relates a particle's spin quantum number, the main magnetic field strength, and a particle's *excitation frequency* and *precession frequency*.

If B is the magnetic field strength and ω is the excitation frequency or the precession frequency then the gyromagnetic ratio γ is found by

$$\gamma = \frac{\omega}{B} \tag{A.1}$$

A.1.3 Excitation

Once aligned with the main magnetic field, net magnetization of a given voxel responds classically to changes in the external magnetic field. A resonant radiofrequency pulse with a magnetic field transverse to the net magnetization's original orientation exerts a torque that rotates the magnetization off its original orientation. This is why MRI scanners employ small antennas and wire loops. They emit the necessary radio waves to rotate the net magnetization vector. Using rf fields to rotate the net magnetization vector is called *excitation*.

Excitation is frequency dependant. This means that the magnetization vector only rotates out of alignment when the rf field oscillates at a certain frequency, called the *resonant frequency*. This frequency can be derived from Eq. (A.1)

$$\omega = \gamma B \tag{A.2}$$

where γ is the gyromagnetic ratio and B is the strength of the main magnetic field at the voxel.

The total angle the magnetization rotates from its original orientation (flip angle) during excitation is given by

$$\alpha = \gamma \int_0^\tau B_1 dt. \tag{A.3}$$

where, again, γ is the gyromagnetic ratio, B_1 is the strength of the magnetic field of the transverse rf pulse, and τ is the duration of the rf pulse.

Flip angle variations generally arise from two sources. First, variations in B_1 strength directly alter the flip angle. A weaker rf field leads to smaller flip angles. Second, variations in main field strength, B_0 , alter the tissue's resonant frequency. With the frequency of the rf pulse different than the resonant frequency, the rf pulse becomes less effective at rotating the tissue magnetization.

A.1.4 Precession

When a compass is perturbed from its alignment with a magnetic field, it oscillates back and forth as it gradually returns to the original orientation. When tipped from its original orientation by an rf field, the net magnetization also oscillates back and forth, only in a three dimensional manner: it oscillates about the main magnetic field direction. This 3D oscillation is called precession.

The angular frequency ω at which the excited magnetization vector precesses about the B0 field is given by

$$\omega = \gamma B \tag{A.4}$$

Notice that precession frequency and excitation frequency are given by the same equation. Actually, the precession rate determines the excitation frequency. RF fields that oscillate at frequencies other than the precession frequency exert torques that counter the precession of the magnetization, causing the precession motion to quickly decay and the magnetization to return to its original alignment. Only on-resonant or nearly on-resonant frequencies exert torques that contribute to the precessional motion of the magnetization vector.

Variations in main field strength cause a voxel's net magnetization to precess at a rate different than its neighbors. This precession plays a crucial role in the phase-sensitive flip-angle mapping technique.

A.1.5 Decay and Relaxation

Once excited and precessing, the magnetization gradually returns to its original orientation. This phenomenon is best described by two processes. *Longitudinal relaxation*, or *T1 relaxation*, marks how the magnetization component that lies along the main magnetic field direction returns to its original magnitude before excitation.

Transverse decay, or *T2 decay*, marks how the magnetization components that are transverse to the main magnetic field decay away.

Longitudinal decay occurs when thermal interactions between precessing nuclei transfer energy throughout the tissue until the entire system of microscopic magnets settles into the lowest energy state: a small majority of nuclei oriented along the B0 field. This longitudinal component $M'_L(t)$ decays exponentially and is governed by the decay constant T1:

$$M'_L(t) = M_0(1 - e^{-t/T1}) + M_{Lo}e^{-t/T1} \quad (\text{A.5})$$

where M_{Lo} is the longitudinal magnetization just after excitation and M_0 is the magnetization just before excitation.

Meanwhile, transverse decay occurs as the magnetization from adjacent nuclei gradually accrue phase relative to each other. Eventually, their respective magnetization vectors cancel out any net magnetization in the xy plane. This effect is governed by the decay constant T2:

$$M'_{xy}(t) = M_{xy}e^{-t/T2} \quad (\text{A.6})$$

where $M'_{xy}(t)$ is the current transverse magnetization strength and M_{xy} is the magnetization just after excitation.

A.2 Pulse Sequences

Acquiring an MRI image requires precise coordination between rf pulses, induced variations in the B0 field called gradients, and readout timing. A *pulse sequence* details the combination and timing of these events as data is collected. Different pulse sequences can have drastically different effects on an image. Pulse sequencing (the process of designing a pulse sequence) is almost an art unto itself. This thesis uses many terms that belong to pulse sequencing and will be explained below.

A.2.1 The Basic Sequence

A pulse sequence consists of four basic components: *excitation*, *encoding*, *readout*, and *relaxation*.

Excitation was discussed in section A.1.3 and will not be discussed here.

Encoding refers to purposefully altering the main magnetic field in order to encode spatial location into a magnetization's precession frequency and overall phase. These field alterations are called *gradients*. The gradient pattern used while encoding has slight influence on the flip angle dual-angle or phase-sensitive flip-angle mapping. However, it has everything to do with the *EPI* sequence employed to capture the phantom and *in vivo* images.

Readout refers to the method and time when the rf coil is switched from transmit mode to receive mode. At this moment, the precessing magnetization vectors inside the tissue induce voltage in the coil. Readout consists of recording this signal and processing it into an image.

Relaxation denotes a time after readout where the main field, rf field, and readout device are all switched off. This period allows the tissue magnetization vectors to relax and reset to their original orientation.

A.2.2 Time Periods

Often one readout session is insufficient to record a complete set of data. A complete image usually requires multiple excitation-encoding-readout-relaxation iterations. Pulse sequencers have come up with a specific set of vocabulary that defines crucial time periods within a pulse sequence:

The *repetition time*, TR, denotes the time between subsequent excitations.

The *echo time*, TE, denotes the time between excitation and readout. It is called

echo time because the encoding patterns are designed to give the signal an extra boost (or echo) at the moment of readout.

The *acquisition time*, TA, denotes the total time needed to acquire an image. Practical sodium flip-angle mapping maintains a TA under ten minutes.

A.3 Glossary of Terms

B0 Field: The main magnetic field produced by an MRI scanner. It is typically between 1-3 tesla.

B1 Field: The transverse, alternating magnetic field associated with a radiofrequency pulse. It is used to rotate nuclei's magnetization vectors out of the equilibrium position.

B1 Map: An image where each voxel records the B1 strength at that particular location.

Bloch Equations: A series of classical equations that describe tissue's net magnetization throughout different processes common to MRI.

EPI: Echo Planar Imaging. Refers to a particular gradient pattern used to encode image information. Used to obtain the flip angle maps used in this thesis.

Flip Angle: The angle formed between the net magnetization's original orientation and its final orientation after excitation by an rf pulse.

FOV: Field of View. The spatial dimensions that an MRI image covers.

Gradient: Purposeful variations in the B0 field that help encode image information prior to readout.

Gyromagnetic Ratio: The ratio relating a nucleus's quantum spin to its magnetization. It plays a pivotal role in most MRI processes.

In Vivo: Latin term used to describe MRI scans of living tissue.

Matrix Size: The dimensions, in voxels, of an MRI image.

Phantom: Any device used to mimic tissue. In this thesis, it is a water bottle doped with physiologic concentrations of sodium.

Pulse Sequence: The pattern and timing of events used to acquire an MRI image.

Readout Bandwidth: Range of frequencies to which the receiving coil remains sensitive.

Readout Duration: See TA

Resolution: Number of voxels within a unit of volume. The higher the resolution, the more voxels needed to image a given volume of space. Further, the higher the resolution, the more fine detail the image is able to show.

Scan Time: See TA

T1 Relaxation: Also called *longitudinal relaxation*. The process where the component of the precessing magnetization vector aligned along the B0 field returns to its magnitude prior to excitation. The process is described by Eq. (A.5).

T2 Decay: Also called *transverse decay*. The process where the transverse components of the precessing magnetization decay exponentially to zero. The process is described by Eq. (A.6)

SNR: Signal to Noise Ratio. A ratio that relates signal magnitude to noise magnitude.

TA: Acquisition Time. Total time required by a pulse sequence to acquire an image.

TE: Echo Time. Time between excitation and readout in a given pulse sequence.

TR: Repetition Time. Time between subsequent excitations in a given pulse sequence.

Voxel: A three-dimensional volume of tissue. An MRI image divides the imaged

object into these discrete volumes.

Bibliography

- [1] A. Borthakur, E. Shapiro, J. Beers, S. Kudchodkar, J. Kneeland, and R. Reddy, “Sensitivity of MRI to proteoglycan depletion in cartilage: comparison of sodium and proton MRI,” *Osteoarthr. Cartilage* **8**, 288–293 (2000).
- [2] J. N. Rydberg, S. J. Riederer, C. Rydberg, and C. Jack, “Contrast Optimization of Fluid Attenuated Inversion Recovery (FLAIR) Imaging,” *Magn Reson Med* **34**, 868–877 (1995).
- [3] A. Wheaton, A. Borthakur, G. Dodge, B. Kneeland, H. Schumacher, and R. Reddy, “Sodium magnetic resonance imaging of proteoglycan depletion in an in vivo model of osteoarthritis,” *Acad. Radiol* **11**, 21–28 (2004).
- [4] A. Wheaton, A. Borthakur, E. Shapiro, R. Regatte, S. Akella, J. Kneeland, and R. Reddy, “Proteoglycan loss in human knee cartilage: quantitation with sodium MR imaging - feasibility study,” *Radiology* **231**, 900–905 (2004).
- [5] R. Ouwerkerk, K. Bleich, J. Gillen, M. Pomper, and P. Bottomley, “Tissue sodium concentration in human brain tumors as measured with ^{23}Na MR imaging,” *Radiology* **227**, 529–537 (2003).

-
- [6] N. Maril, Y. Rosen, G. Reynolds, A. Ivanishev, L. Ngo, and R. Lenkinski, “Sodium MRI of the human kidney at 3 tesla.,” *Magn Reson Med* **56**, 1229–1234 (2006).
- [7] Y. Rosen and R. E. Lenkinski, “Sodium MRI of a human transplanted kidney.,” *Acad. Radiol* **16**, 886–889 (2009).
- [8] K. R. Thulborn, D. Davis, J. Snyder, H. Yonas, and A. Kassam, “Sodium MR imaging of acute and subacute stroke for assessment of tissue viability.,” *RNeuroimaging Clin N Am* **15**, 302–309 (2005).
- [9] R. Ouwerkerk, M. Jacobs, J. Macura, A. Wolff, V. Stearns, S. Mezban, N. Khouri, D. Bluemke, and P. Bottomley, “Elevated tissue sodium concentration in malignant breast lesions detected with non-invasive ^{23}Na MRI,” *Radiology* **106**, 151–160 (2007).
- [10] V. Yushmanov, B. Yanovski, A. Kharlamov, G. LaVerde, F. Boada, and S. Jones, “Sodium mapping in focal cerebral ischemia in the rat by quantitative (^{23}Na) MRI,” *Magn Reson Imaging* **29**, 9626 (2009).
- [11] G. Morrell, “A phase-sensitive method of flip angle mapping,” *Magn Reson Med* **60**, 889–894 (2008).
- [12] E. Insko and L. Bollinger, “Mapping of the radiofrequency field,” *J Magn Reson* **103**, 82–85 (1993).
- [13] C. Cunningham, J. Pauly, and K. Nayak, “Saturated double-angle method for rapid $B1+$ mapping,” *Magn Reson Med*, volume = 57, pages = 192-2000, year = 2007, .

-
- [14] R. Stollberger and P. Wach, “Imaging of the active B1 field in vivo,” *Magn Reson Med* **35**, 245–251 (1996).
- [15] D. Nishimura, *Principles of Magnetic Resonance Imaging* (Published by Author, 2010).
- [16] M. Bernstein, K. King, and X. Zhou, *Handbook of MRI Pulse Sequences* (Elsevier Inc, 2004).
- [17] F. Boada, G. S. J.S. Gillen, S. Chang, and K. Thulborn, “Tissue sodium concentration in human brain tumors as measured with ^{23}Na MR imaging,” *Magn Reson Med* **37**, 706–715 (2005).
- [18] L. Lesperance, M. Gray, and D. Burstein, “Determination of Fixed Charge Density in Cartilage Using Nuclear Magnetic Resonance,” *J Orthop Res* pp. 1–13 (1992).
- [19] Y. Qian, V. Stenger, and F. Boada, “Parallel imaging with 3D TPI trajectory: SNR and acceleration benefits,” *Magn Reson Imaging* **27**, 656–663 (2009).
- [20] A. Nagel, F. Laun, M. Weber, C. Matthies, W. Semmler, and L. Schad, “Sodium MRI using a density-adapted 3D radial acquisition technique,” *Magn Reson Med* **62**, 1565–1573 (2009).
- [21] P. Gurney, B. Hargreaves, and D. Nishimura, “Design and analysis of a practical 3D cones trajectory,” *Magn Reson Med* **55**, 575–582 (2006).

Index

B0 field inhomogeneity, 6
B1 map, 2
Bloch equations, 11, 32

cartilage, 1

dual-angle technique, 4

encoding, 36
EPI, 17, 36
excitation, 11, 33, 36

flip angle, 3, 33
FOV, 18

gradient, 36
gyromagnetic ratio, 3, 8

in vivo, 8, 11

longitudinal relaxation, 11, 34

matrix size, 18
Monte Carlo, 10

net magnetization, 32

phantom, 8, 10
phase-sensitive technique, 4
precession, 11
precession frequency, 32
pulse sequence, 27, 36

quantum numbers, 31

readout, 36
readout bandwidth, 18
readout duration, 18
receiver coil, 13

resolution, 18
resonant frequency, 33
rf field, 1

SNR, 2, 18
spin, 31

T1 relaxation, 11, 34
T2 decay, 11, 35
TA, 37
TE, 27, 36
TR, 36
transverse decay, 11, 35

voxel, 11, 32